Remote sensing of the ocean contributions from ultraviolet to near-infrared using the shortwave infrared bands: simulations

Menghua Wang

In the remote sensing of the ocean near-surface properties, it is essential to derive accurate water-leaving radiance spectra through the process of the atmospheric correction. The atmospheric correction algorithm for Sea-Viewing Wide Field-of-View Sensor (SeaWiFS) and Moderate Resolution Imaging Spectroradiometer (MODIS) uses two near-infrared (NIR) bands at 765 and 865 nm (748 and 869 nm for MODIS) for retrieval of aerosol properties with assumption of the black ocean at the NIR wavelengths. Modifications are implemented to account for some of the NIR ocean contributions for the productive but not very turbid waters. For turbid waters in the coastal regions, however, the ocean could have significant contributions in the NIR, leading to significant errors in the satellite-derived ocean water-leaving radiances. For the shortwave infrared (SWIR) wavelengths ($\gtrsim$1000 nm), water has significantly larger absorption than those for the NIR bands. Thus the black ocean assumption at the SWIR bands is generally valid for turbid waters. In addition, for future sensors, it is also useful to include the UV bands to better quantify the ocean organic and inorganic materials, as well as for help in atmospheric correction. Simulations are carried out to evaluate the performance of atmospheric correction for nonabsorbing and weakly absorbing aerosols using the NIR bands and various combinations of the SWIR bands for deriving the water-leaving radiances at the UV (340 nm) and visible wavelengths. Simulations show that atmospheric correction using the SWIR bands can generally produce results comparable to atmospheric correction using the NIR bands. In particular, the water-leaving radiance at the UV band (340 nm) can also be derived accurately. The results from a sensitivity study for the required sensor noise equivalent reflectance, (NE$\Delta\rho$), [or the signal-to-noise ratio (SNR)] for the NIR and SWIR bands are provided and discussed. © 2007 Optical Society of America

OCIS codes: 010.0010, 280.0280, 010.1110, 290.0290.

1. Introduction

The total reflectance $\rho_t(\lambda)$ measured at the top of the atmosphere (TOA) at a wavelength λ can basically be decomposed as from various reflectance contributions[1,2]:

$$\rho_t(\lambda) = \rho_r(\lambda) + \rho_A(\lambda) + t(\lambda)\rho_w(\lambda), \tag{1}$$

where $\rho_r(\lambda)$ is the Rayleigh reflectance from multiple scattering by air molecules,[3–6] $\rho_A(\lambda)$ is the aerosol reflectance (including Rayleigh–aerosol interactions[7]) from multiple scattering by particles,[1] and $\rho_w(\lambda)$ is the ocean water-leaving reflectance. The term $t(\lambda)$ is the diffuse transmittance[8] at the sensor viewing angle. For brevity in the discussion, the reflectance contributions from sun glint[9,10] and ocean whitecaps[11–13] are ignored. To derive the ocean water-leaving reflectance spectra $\rho_w(\lambda)$ from Eq. (1), the atmospheric and ocean surface effects, i.e., $\rho_r(\lambda)$ and $\rho_A(\lambda)$, have to be removed. The current atmospheric correction algorithm for Sea-viewing Wide Field-of-View Sensor (SeaWiFS)[14] and Moderate Resolution Imaging Spectroradiometer (MODIS)[15] computes the Rayleigh reflectance $\rho_r(\lambda)$ from the Rayleigh lookup tables with inputs of the solar-sensor geometry, atmospheric pressure, and wind speed.[3–6] The aerosol reflectance $\rho_A(\lambda)$ is estimated using two near-infrared (NIR) bands at 765 and 865 nm (748 and 869 nm for MODIS) with assumption of the black ocean at the NIR wavelengths. The NIR black ocean assumption is usually valid at the open oceans where the ocean optical properties are mainly as a function of the pigment concentration with

M. Wang is with the National Oceanic and Atmospheric Administration, National Environmental Satellite, Data, and Information Service, the Center for Satellite Applications and Research, E/RA3, Room 102, 5200 Auth Road, Camp Springs, Maryland 20746. His e-mail address is menghua.wang@noaa.gov.

Received 4 August 2006; accepted 24 October 2006; posted 10 November 2006 (Doc. ID 73773); published 1 March 2007.

0003-6935/07/091535-13$15.00/0

© 2007 Optical Society of America

generally low pigment concentration value. However, for high productive ocean waters (e.g., pigment concentration $> \sim 2$ mg/cm^3) and for turbid waters in the coastal regions (e.g., waters with high sediment concentration), the NIR $\rho_w(\lambda)$ contributions are no longer negligible[16–18] and can be very significant.[19] In these cases, atmospheric correction often results in significant error in the derived $\rho_w(\lambda)$ values, i.e., an overestimation of $\rho_A(\lambda)$ contributions and therefore underestimation of $\rho_w(\lambda)$ values [see Eq. (1)].[16,19] This is basically because at the NIR wavelengths water absorptions are not large enough to absorb photons backscattered by particles from the oceans.

The current SeaWiFS and MODIS atmospheric correction algorithm has employed a method to account for the NIR ocean contributions[17,20] based on a model of the spectral shape for the particle backscattering coefficient in coastal waters.[16,18,21,22] Over the turbid ocean waters, however, there are still significant errors in the satellite-derived ocean color products because of model limitations for the complex turbid waters. For wavelengths longer than the NIR band, water absorption increases very rapidly as the increase of wavelength. Indeed, for the shortwave infrared (SWIR) wavelengths ($\gtrsim$1000 nm), water has much stronger absorption than that at 865 nm.[23,24] Specifically, from Hale and Querry[23] (1973), the water absorption coefficients for wavelengths 865, 1000, 1240, 1640, and 2130 nm are approximately 5, 36, 88, 498, and 2228 m^{-1}, respectively. Therefore, with the black ocean assumption, the SWIR bands can be used for detecting turbid waters[25] as well as for atmospheric correction in the coastal ocean regions.[19,26,27]

With the derived ocean water-leaving reflectance spectra $\rho_w(\lambda)$, the ocean in-water optical properties, e.g., ocean inherent optical property (IOP) and chlorophyll-*a* concentration, can be inferred.[28–30] Both SeaWiFS and MODIS have been providing the ocean water-leaving radiance spectra covering from 412 to 670 nm.[14,31] The $\rho_w(\lambda)$ value at 443 nm is sensitive to the change of the phytoplankton pigment concentration because phytoplankton absorption peaks at approximately 443 nm.[32] The absorption of inorganic materials (e.g., phytoplankton) decreases with a decrease of the wavelength, dropping off very significantly below 400 nm. In contrast, the absorption by ocean organic materials, e.g., colored dissolved organic matter (CDOM), increases rapidly with decrease of wavelength into the ultraviolet (UV) region (340–400 nm).[33,34] The absorption divergence between the organic and inorganic materials in the ocean is most significant at the UV wavelength domain, and can be possibly used to quantify these two major components from satellite sensors. On the other hand, the UV bands can be used for detecting the strongly absorbing aerosols and deriving their optical properties[35] for atmospheric correction.

For remote sensing of ocean properties from satellite sensors, the sensor spectral bands are usually located in atmospheric windows, thereby maximizing sensitivity in sensor-measured radiance to the variation of the observing target and reducing atmospheric absorption effects that lead to uncertainty in the derived optical and geophysical products. Figure 1 provides an example of the transmittance of the atmosphere (looking toward the zenith) as a function of wavelength (from 300 to 2200 nm). The atmospheric transmittance values are derived by using LOWTRAN-7 for the 1976 U.S. standard atmosphere model.[36,37] Figure 1 shows the absorption features from the main atmospheric constituent of O_2, O_3, H_2O, and CO_2 for wavelengths 300–2200 nm. In addition to the NIR bands, atmospheric windows in the SWIR bands are shown to be at approximately 1000, 1240, 1640, and 2130 nm. In fact, MODIS has the SWIR bands at 1240, 1640, and 2130 nm, which were designed for land and atmosphere applications. For the UV region, the useful radiance with the shortest wavelength for ocean color remote sensing is at approximately 340 nm due to extremely strong absorption by ozone for wavelengths <340 nm. Thus the UV wavelength region between 340 and 400 nm can possibly be added for future ocean color satellite sensors.

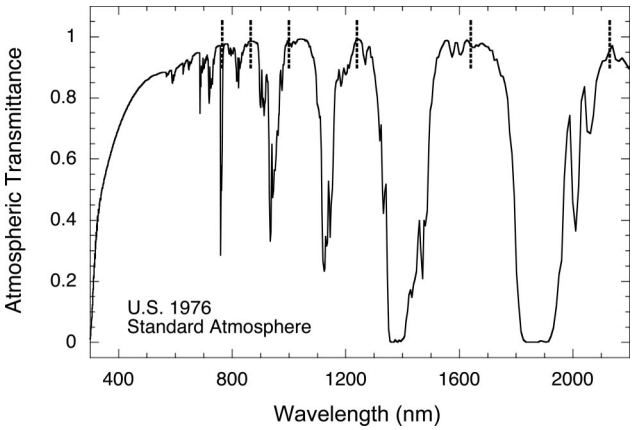

Fig. 1. Atmosphere transmittance as a function of the wavelength derived from LOWTRAN-7 using the 1976 U.S. standard atmosphere model.

In this paper, simulations are carried out to evaluate and compare the performance of atmospheric correction for nonabsorbing and weakly absorbing aerosols using the NIR bands and various combinations of the SWIR bands for deriving the water-leaving reflectance spectra from the UV to the visible wavelengths. The algorithm evaluations are similar to the work carried out by Gordon and Wang[1] (1994) for the NIR algorithm, which have been validated with various *in situ* data for SeaWiFS and MODIS measurements.[14,38,39] Specifically, the results from the atmospheric correction algorithm using combinations of the two SWIR bands of 1000 and 1240 nm, 1240 and 1640 nm, 1240 and 2130 nm, and 1640 and 2130 nm are evaluated and compared with those using the two NIR bands of 765 and 865 nm. The derived products include the ocean water-leaving

reflectance spectra and aerosol products. In particular, algorithm performance in retrieval of the ocean contributions at the UV (340 nm) and NIR bands using the SWIR band method is evaluated. Finally, a sensitivity study to understand sensor noise effects on the performance of atmospheric correction algorithm using the NIR and various combinations of the SWIR bands is conducted, leading to recommendations for the sensor signal-to-noise ratio (SNR) requirements for the NIR and SWIR bands.

2. Aerosol Lookup Tables for Ultraviolet and Short-wave Infrared Bands

The Gordon and Wang[1] (1994) algorithm has been implemented in the SeaWiFS and MODIS ocean color data processing system through the use of the lookup tables. The Rayleigh reflectance $\rho_r(\lambda)$ in Eq. (1) can be computed quite accurately from the Rayleigh lookup tables with inputs of the solar-sensor geometry, atmospheric pressure, and ocean surface wind speed.[3–6] The aerosol lookup tables, however, were generated based on the scalar radiative transfer equation (neglecting the polarization effects) for a two-layer plane-parallel atmosphere (PPA) overlying a flat Fresnel-reflecting ocean surface[1,4] and for a set of 12 aerosol models.[40] The aerosol polarization effects are discussed in detail in a recent study.[41] The 12 aerosol models used for the SeaWiFS and MODIS ocean color data processing are from, or derived from, the work of Shettle and Fenn.[42] Specifically, they are the oceanic model with the relative humidity (RH) of 99% (O99), the maritime model with RH of 50%, 70%, 90%, and 99% (M50, M70, M90, and M99), the coastal model with RH of 50%, 70%, 90%, and 99% (C50, C70, C90, and C99), and the tropospheric model with RH of 50%, 90%, and 99% (T50, T90, and T99).[1,40,42] The *in situ* measurements from various ocean regions show that these aerosol models are reasonably representative of ocean maritime environments.[40,43–45]

For this work, in addition to the 12 aerosol model data for the SeaWiFS and MODIS ocean spectral bands, the aerosol optical property data for the 12 aerosol models were also generated using Mie theory assuming spherical particles for spectral bands at 340, 1000, 1240, 1640, and 2130 nm. Similar to the generation of the SeaWiFS and MODIS aerosol lookup tables, the aerosol lookup tables for the UV and SWIR bands were generated using the radiative transfer simulations that were carried out with the 12 aerosol models for nine aerosol optical thicknesses (0.02, 0.05, 0.1, 0.15, 0.2, 0.3, 0.4, 0.6, and 0.8), 33 solar-zenith angles from 0° to 80° at steps of 2.5°, and 35 sensor-zenith angles from 1° to 75° at steps of ~2°. We define the aerosol single-scattering epsilon (SSE) parameter $\varepsilon(\lambda, \lambda_0)$ as the ratio of the aerosol single-scattering reflectance $\rho_{as}(\lambda)$ between two bands,[1,46,47] i.e.,

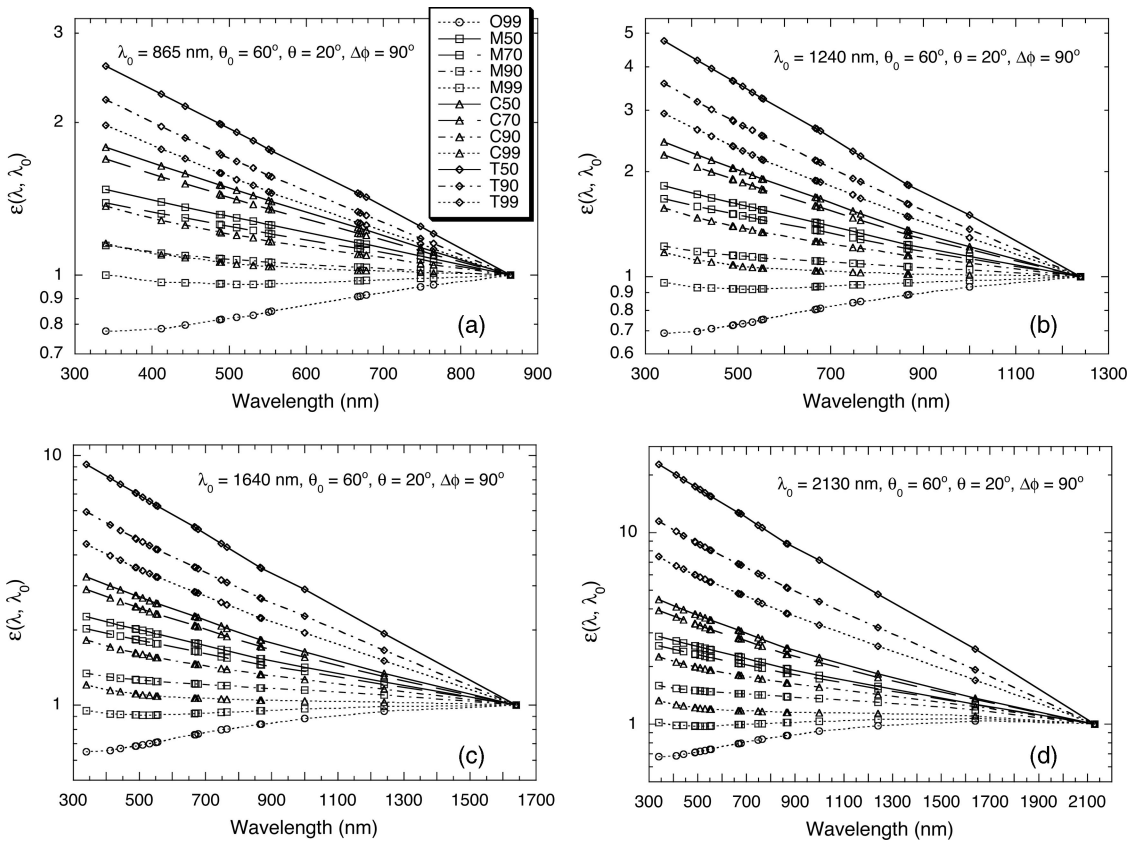

Fig. 2. Single-scattering epsilon $\varepsilon(\lambda, \lambda_0)$ as a function of the wavelength for the 12 aerosol models and for the reference wavelength at (a) 865 nm, (b) 1240 nm, (c) 1640 nm, and (d) 2130 nm.

$$\varepsilon(\lambda,\ \lambda_0) = \frac{\rho_{as}(\lambda)}{\rho_{as}(\lambda_0)} \equiv \frac{\omega_a(\lambda)c_{ext}(\lambda)p_a(\theta_0,\ \theta,\ \Delta\phi,\ \lambda)}{\omega_a(\lambda_0)c_{ext}(\lambda_0)p_a(\theta_0,\ \theta,\ \Delta\phi,\ \lambda_0)}, \tag{2}$$

where $\omega_a(\lambda)$, $c_{ext}(\lambda)$, and $p_a(\theta_0, \theta, \Delta\phi, \lambda)$ are the aerosol single-scattering albedo, the aerosol extinction coefficient, and the aerosol effective scattering phase function,[1] respectively. The SSE depends mainly on the aerosol model and can be used to characterize the aerosol spectral variation for various aerosol models.[1] Figure 2 provides examples of the SSE as a function of the wavelength (from the UV to NIR or to various SWIR bands) for the 12 aerosol models. Figures 2(a)–2(d) show the SSE $\varepsilon(\lambda, \lambda_0)$ at the reference wavelengths λ_0 of 865, 1240, 1640, and 2130 nm, respectively. They are all for the case of a solar-zenith angle of 60°, sensor-zenith angle of 20°, and relative-azimuth angle of 90°. As expected, the $\varepsilon(\lambda, \lambda_0)$ value has significant variations corresponding to various reference wavelength λ_0 values. Between the O99 and the T50 models (from the lowest to the highest SSE values), Fig. 2 shows that the SSE values at the UV band for $\varepsilon(340, 865)$, $\varepsilon(340, 1240)$, $\varepsilon(340, 1640)$, and $\varepsilon(340, 2130)$ are in the ranges of 0.8–2.6, 0.7–4.8, 0.7–9.2, and 0.7–22.6, respectively. Particularly, the NIR and SWIR SSE values of $\varepsilon(765, 865)$, $\varepsilon(1000, 1240)$, $\varepsilon(1240, 1640)$, $\varepsilon(1240, 2130)$, and $\varepsilon(1640, 2130)$, which are used for the selection of aerosol models in atmospheric correction,[1] are in the ranges of 0.96–1.21, 0.93–1.50, 0.95–1.94, 0.98–4.76, and 1.04–2.46, respectively. Obviously, there are significantly higher measurement sensitivities in the SSE with the SWIR bands where there is a substantially larger apart of wavelength distance between two bands, e.g., $\varepsilon(1240, 2130)$.

The implementation of the aerosol lookup tables into the data processing system can be achieved by relating the aerosol reflectance $\rho_A(\lambda)$ to its corresponding single-scattering aerosol reflectance $\rho_{as}(\lambda)$,[41] i.e.,

$$\rho_A(\lambda_j,\ \theta_0,\ \theta,\ \Delta\phi,\ \tau_a) = \sum_{i=0}^{4} a_i(\lambda_j,\ \theta_0,\ \theta,\ \Delta\phi) \times [\rho_{as}(\lambda_j,\ \theta_0,\ \theta,\ \Delta\phi,\ \tau_a)]^i, \tag{3}$$

where $a_i(\lambda_j, \theta_0, \theta, \Delta\phi)$ are coefficients to fit fourth power polynomial for $\rho_A(\lambda_j, \theta_0, \theta, \Delta\phi, \tau_a)$ as a function of $\rho_{as}(\lambda_j, \theta_0, \theta, \Delta\phi, \tau_a)$ in the least square for all spectral bands λ_i from the UV to the SWIR and for the solar-zenith angle θ_0 from 0° to 80° at every 2.5°, the sensor-zenith angle θ from 1° to 75° at every ~2°, and the relative-azimuth angle θ_0 from 0° to 180° at every 10°. The coefficients $a_i(\lambda_j, \theta_0, \theta, \Delta\phi)$ were derived by fitting the curves that were obtained from data simulated with aerosol optical thicknesses $\tau_a(\lambda)$ of 0.02, 0.05, 0.1, 0.15, 0.2, 0.3, 0.4, 0.6, and 0.8 for the 12 aerosol models. On the other hand, the sensor-measured NIR or SWIR aerosol reflectances need to be converted to the aerosol single-scattering reflectance for atmospheric correction as well as for retrieval of aerosol optical properties.[1] Therefore, coefficients were also generated for computing the aerosol single-scattering reflectance $\rho_{as}(\lambda)$ as a function of the aerosol reflectance $\rho_A(\lambda)$ at the NIR and SWIR bands, i.e.,

$$\rho_{as}(\lambda_j,\ \theta_0,\ \theta,\ \Delta\phi,\ \tau_a) = \sum_{i=0}^{4} b_i(\lambda_j,\ \theta_0,\ \theta,\ \Delta\phi) \times [\rho_A(\lambda_j,\ \theta_0,\ \theta,\ \Delta\phi,\ \tau_a)]^i, \tag{4}$$

where $b_i(\lambda_j, \theta_0, \theta, \Delta\phi)$ are coefficients to fit fourth power polynomial for $\rho_{as}(\lambda_j, \theta_0, \theta, \Delta\phi, \tau_a)$ as a function of $\rho_A(\lambda_j, \theta_0, \theta, \Delta\phi, \tau_a)$ in the least square for the NIR and SWIR bands, i.e., 765, 865, 1000, 1240, 1640, and 2130 nm. Directly calculating $\rho_{as}(\lambda_j, \theta_0, \theta, \Delta\phi, \tau_a)$ using Eq. (4) instead of solving Eq. (3), eliminates uncertainty and increases the computing efficiency in numerical solution for the high-order polynomials [Eq. (3)]. These methods [Eqs. (3) and (4)] are accurate and efficient in the data processing. Therefore, the aerosol lookup tables are generated as in the forms with which coefficients $a_i(\lambda_j, \theta_0, \theta, \Delta\phi)$ (for all spectral bands from the UV to the SWIR) and $b_i(\lambda_j, \theta_0, \theta, \Delta\phi)$ (for the NIR and SWIR bands) are stored for the solar-zenith angles from 0° to 80° at

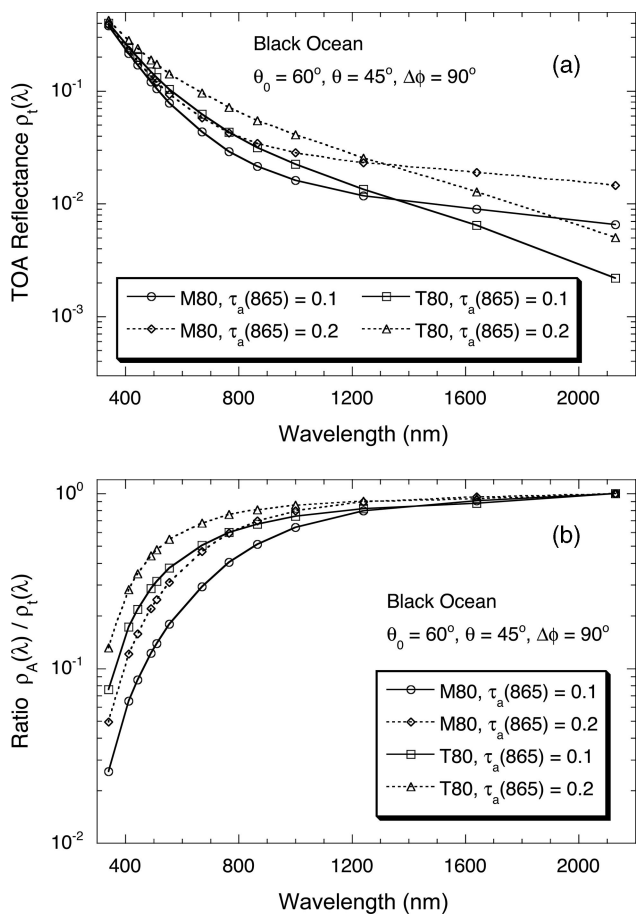

Fig. 3. Simulated (a) TOA reflectance $\rho_t(\lambda)$ and (b) ratio of the TOA aerosol reflectance to the total reflectance $\rho_A(\lambda)/\rho_t(\lambda)$ as a function of the wavelength from 340 to 2130 nm for the case of the black ocean and for aerosol models of the M80 and the T80 with aerosol optical thicknesses at 865 nm of 0.1 and 0.2.

steps of 2.5°, the sensor-zenith angles from 1° to 75° at steps of ~2°, and the relative-azimuth angles from 0° to 180° at steps of 10°. For any given solar-sensor geometry, a linear interpolation (three-dimension) is carried out to produce the corresponding coefficients $a_i(\lambda_j, \theta_0, \theta, \Delta\phi)$ and $b_i(\lambda_j, \theta_0, \theta, \Delta\phi)$ for computations of $\rho_A(\lambda_j, \theta_0, \theta, \Delta\phi, \tau_a)$ at the UV to the SWIR bands and $\rho_{as}(\lambda_j, \theta_0, \theta, \Delta\phi, \tau_a)$ at the NIR or SWIR bands.

3. Algorithm Performance Comparison with Simulations

In this section, the results from atmospheric correction and aerosol retrievals using the NIR and various combinations of the SWIR bands for the derivation of water-leaving reflectance spectra in the UV and in the visible wavelengths, as well as for the retrieval of aerosol products, are compared and discussed. The results in the ocean NIR contributions derived from various SWIR bands are also provided.

A. The Pseudo Top of the Atmosphere Reflectances

Figure 3(a) provides examples of the simulated TOA reflectance spectra from 340 to 2130 nm for the case of the black ocean for aerosol models of the Maritime and Tropospheric with a RH of 80% (M80 and T80). The M80 and T80 models represent nonabsorbing and weakly absorbing aerosols with the single-scattering albedo values of 0.99 and 0.95 at 865 nm, respectively. These two models are similar, but not identical, to the 12 aerosol models used in the aerosol lookup tables for the data processing, i.e., we assume that the 12 aerosol models are representative for real situations. In Fig. 3(a), the reflectance spectra were simulated using the scalar radiative transfer computation (neglecting the polarization effects) for a two-layer atmosphere overlying a flat Fresnel-reflecting ocean surface for the M80 and T80 aerosol models with aerosol optical thicknesses at 865 nm $\tau_a(865)$ of 0.1 and 0.2. This is the case for a specific solar-sensor geometry with the solar-zenith angle of 60°, sensor-zenith angle of 45°, and a relative-azimuth angle of 90°. Figure 3(a) shows that the TOA reflectance simulated with the T80 model has a significant spectral variation that the M80 model does not. Indeed, for the T80 model with $\tau_a(865)$ of 0.1, the TOA reflectance ratio between 340 and 2130 nm is ~200, while for the M80 model the ratio value between 340 and 2130 nm is ~60. It is noted, however, that at the 340 nm wavelength the simulated TOA reflectance $\rho_t(\lambda)$ values are similar for various aerosol optical properties (model and aerosol optical thicknesses) because of significantly dominated Rayleigh reflectance contribution at the UV bands [Fig. 3(b)].

Figure 3(b) provides the ratio of the TOA aerosol reflectance to the total reflectance $\rho_A(\lambda)/\rho_t(\lambda)$ as a function of the wavelength from the UV to the SWIR

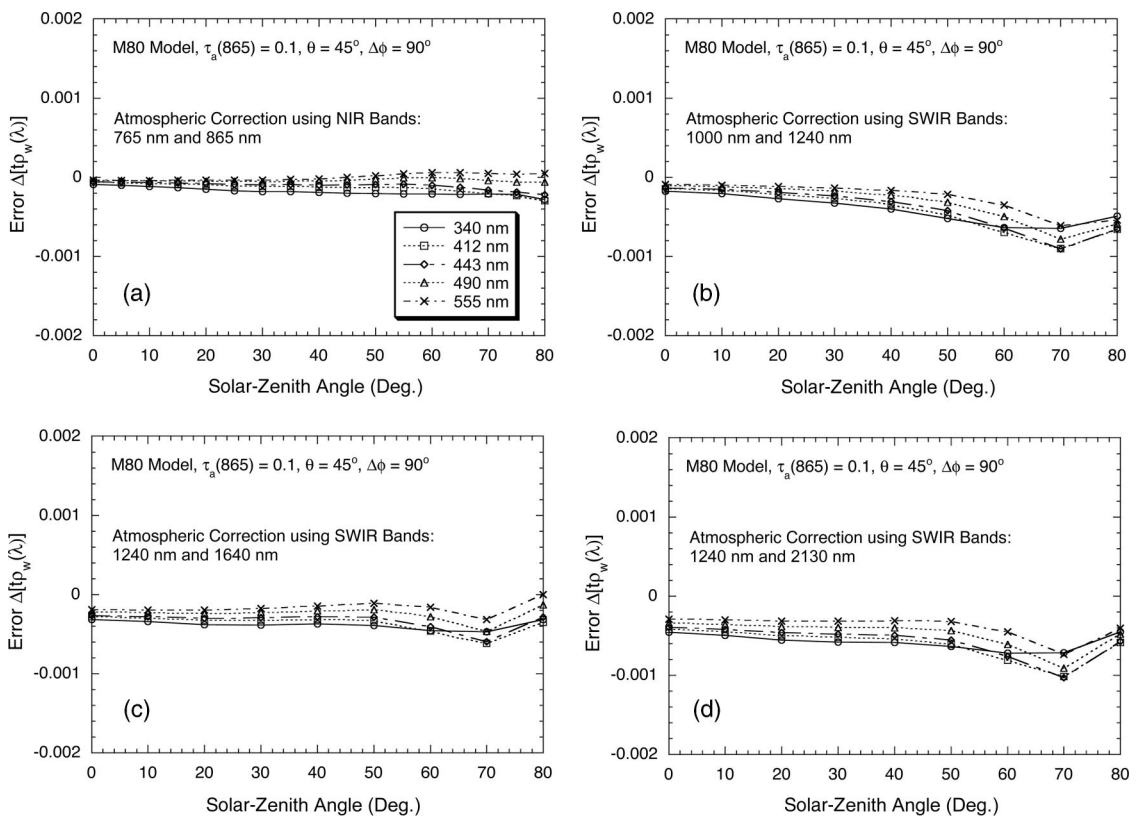

Fig. 4. Error in the derived water-leaving reflectance $[t\rho_w(\lambda)]$ at wavelengths 340, 412, 443, 490, and 555 nm as a function of the solar-zenith angle for the M80 aerosol model with $\tau_a(865)$ of 0.1 and for the algorithm performed using band combinations of (a) 765 and 865 nm, (b) 1000 and 1240 nm, (c) 1240 and 1640 nm, and (d) 1240 and 2130 nm. This is for the case of sensor-zenith angle of 45° and relative-azimuth angle of 90°.

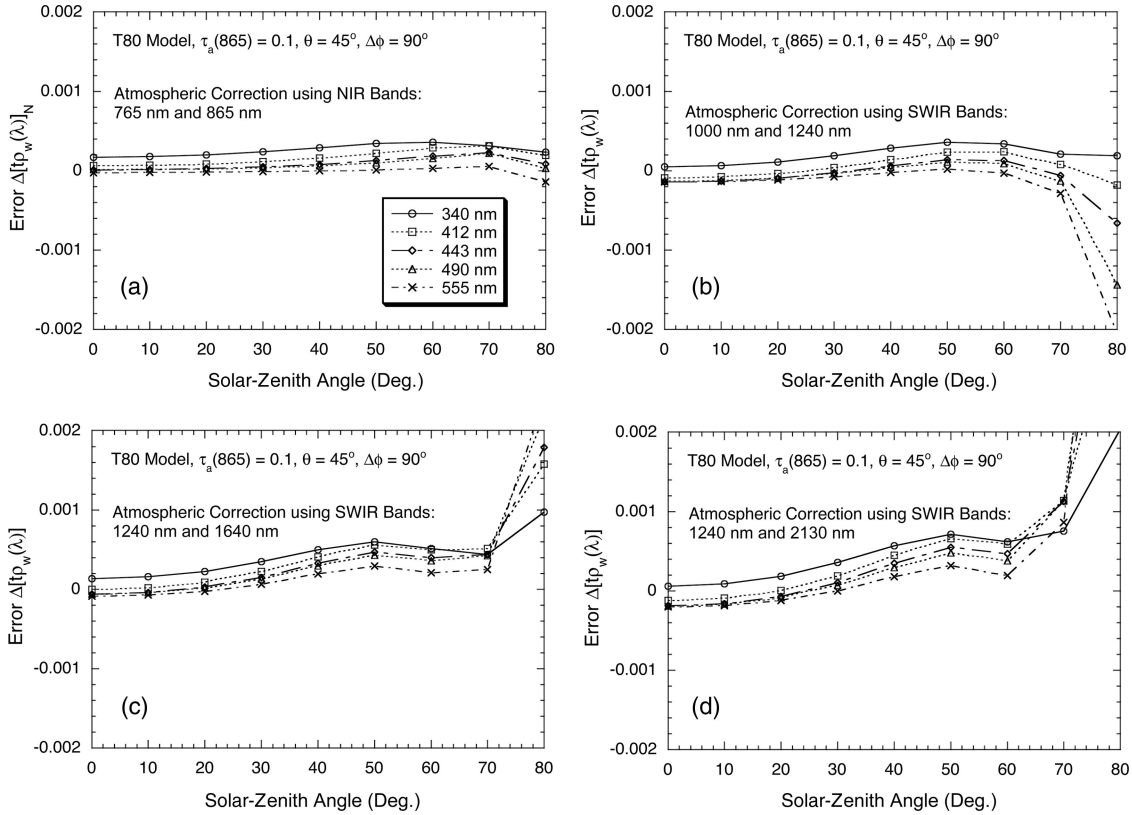

Fig. 5. Same as in Fig. 4 except that data are for the T80 aerosol model.

wavelengths, corresponding to the cases in Fig. 3(a). Figure 3(b) shows that at the UV and short visible bands the sensor-measured signals are really dominated from the contributions of Rayleigh (air molecules) scattering. For the case of the M80 model with $\tau_a(865)$ of 0.1, and assuming a black ocean, the aerosol reflectance $\rho_A(\lambda)$ contributes approximately 2.6%, 6%, 9%, 12%, 18%, 29%, 51% in the TOA reflectance for wavelengths at 340, 412, 443, 490, 555, 670, and 865 nm, respectively, while for the T80 model the corresponding values are approximately 7.6%, 17%, 22%, 29%, 38%, 51%, and 67%, respectively. With the inclusion of the ocean contributions in $\rho_t(\lambda)$, the ratio $\rho_A(\lambda)/\rho_t(\lambda)$ values in the UV and visible wavelengths are even smaller. This underscores the importance of accurately computing the Rayleigh reflectance $\rho_r(\lambda)$, in particular, for the UV and the visible wavelengths.

B. Algorithm Evaluation for the Derived Water-Leaving Reflectance

To understand the algorithm performance in retrieval of the water-leaving reflectance spectra using various combinations of the SWIR bands, simulations have been carried out using the pseudo TOA reflectance simulated with the M80 and the T80 aerosol models as inputs. The outputs from the atmospheric correction algorithm using various combinations of the SWIR bands are compared with the results that are derived from the current SeaWiFS and MODIS algorithm,[1,2] i.e., using the two NIR bands for atmospheric correction. Figures 4 and 5 provide examples of the error in the retrieved water-leaving reflectance $[t\rho_w(\lambda)]$ from the method performed using various combinations of the NIR and SWIR bands. Figures 4(a)–4(d) are the errors in the derived water-leaving reflectance $[t\rho_w(\lambda)]$, for the M80 model with $\tau_a(865)$ of 0.1, as functions of the solar-zenith angle for the algorithm performed using bands of 765 and 865 nm, 1000 and 1240 nm, 1240 and 1640 nm, and 1240 and 2130 nm, respectively, while Figs. 5(a)–5(d) are the corresponding results for the T80 aerosol model. These are all for a case of the sensor-zenith angle of 45° and the relative-azimuth angle of 90°. The results in Fig. 4 show that, for the M80 model, the atmospheric correction performed using the SWIR band combinations of 1000 and 1240 nm, 1240 and 1640 nm, and 1240 and 2130 nm has results comparable with those from the algorithm using the two NIR (765 and 865 nm) bands. The errors in the derived $[t\rho_w(\lambda)]$ are all within 0.001 (usually within ~0.0005) for the UV (340 nm) and visible wavelengths (412, 443, 490, and 555 nm). We can draw similar conclusions for the T80 model for cases with which the solar-zenith angles ≤70° (Fig. 5).

Using combinations of the SWIR bands for atmospheric correction, the water-leaving reflectances at the NIR bands can also be derived. Figure 6 gives examples of the accuracy in the derived water-leaving reflectances at the NIR bands for the M80 and the T80 aerosol models with $\tau_a(865)$ of 0.1. Figures 6(a) and 6(b) are errors in the derived water-leaving reflectance $\Delta[t\rho_w(\lambda)]$ for the M80 aerosols as

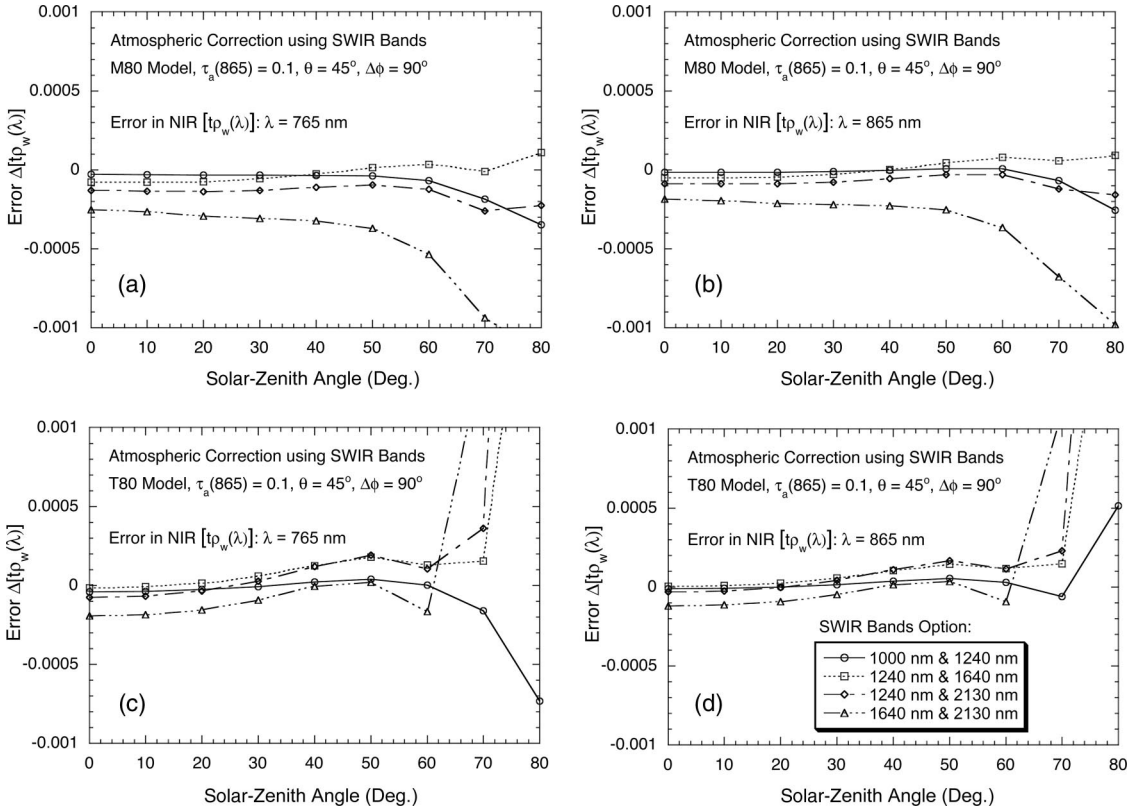

Fig. 6. Error in the derived NIR water-leaving reflectance as a function of the solar-zenith angle for algorithm performed using the SWIR band combinations of 1000 and 1240 nm, 1240 and 1640 nm, 1240 and 2130 nm, and 1640 and 2130 nm and for $\Delta[t\rho_w(\lambda)]$ derived at NIR wavelength with the aerosol model of (a) and (b) 765 and 865 nm with the M80 model and (c) and (d) 765 and 865 nm with the T80 model.

functions of the solar-zenith angle for wavelengths at 765 and 865 nm, respectively, while Figs. 6(c) and 6(d) are the results in $\Delta[t\rho_w(\lambda)]$ for the T80 model for wavelengths at 765 and 865 nm, respectively. In addition to the three combinations of the SWIR bands presented in Figs. 4 and 5, the method using the SWIR bands of 1640 and 2130 nm has also been included in Fig. 6. The results in Fig. 6 show that, except for the method using 1640 and 2130 nm, errors $\Delta[t\rho_w(\lambda)]$ are almost all within uncertainty of $\sim 10^{-4}$ for cases with which the solar-zenith angles $\leq 70°$.

To further assess the algorithm performance and quantify uncertainty using various combinations of the SWIR bands, simulations have been carried out for all applicable solar-sensor geometry with various aerosol optical properties. Simulations have been conducted for cases with the solar-zenith angles from 0° to 80° at steps of 5°, the sensor-zenith angles from 0° to 65° at steps of 5°, and the relative-azimuth angles from 0° to 180° at steps of 10°, and for the M80 and T80 aerosol models with aerosol optical thicknesses 0.05, 0.1, and 0.2 at 865 nm. This is a total of approximately 12,000 cases (excluding sun glint cases) for each aerosol model (M80 or T80). Histograms and statistics for algorithm performance using the NIR bands and various combinations of the SWIR bands are generated and analyzed. Table 1 summarizes all the results that compare algorithm performance with various band options for atmospheric correction. In Table 1, the percentage of cases for a given error range in the derived water-leaving reflectance for various options in atmospheric correction is provided for the M80 and T80 models. For example, for the UV (340 nm) water-leaving reflectance derived using the NIR bands (765 and 865 nm) method, there are 87.0%, 94.4%, and 98.4% of cases with uncertainty $\Delta[t\rho_w(\lambda)]$ within 5×10^{-4}, 1×10^{-3}, and 2×10^{-3} for the M80 model, respectively, while these percentages are 92.9%, 95.5%, and 97.6% for the T80 model. Compared with the results derived from the NIR bands, however, the results from various SWIR band options for atmospheric correction show lower percentage values for the case with the M80 model, while for the T80 model the band option of the 1000 and 1240 nm combination provides results comparable with those from the option of the two NIR bands. It is striking to note that the algorithms with various band combination options performed as well for the short visible bands as for the UV band (340 nm). The water-leaving reflectance at the UV wavelengths (e.g., 340 nm) can be derived accurately because of significantly fewer aerosol reflectance contributions in the UV bands (see Fig. 3).

There are apparently two main factors affecting the performances of atmospheric correction with various band combination options (Table 1): (a) The wavelength distance must be extrapolated for the

Table 1. Algorithm Performance Comparisons Using the NIR and the Various Combinations of SWIR Bands

λ (nm)	Two Bands for Atmospheric Correction (nm)	% Cases for Range of $\lvert\Delta[t\rho_w(\lambda)]\rvert$ ($\times 10^{-3}$)					
		M80 Model			T80 Model		
		≤0.5	≤1.0	≤2.0	≤0.5	≤1.0	≤2.0
340	765 and 865	87.0	94.4	98.4	92.9	95.5	97.6
	1000 and 1240	64.6	82.8	92.7	93.3	95.6	97.6
	1240 and 1640	70.9	84.6	93.8	86.7	92.1	94.7
	1240 and 2130	48.1	71.3	87.7	76.0	84.3	89.8
	1640 and 2130	23.5	45.5	72.7	75.8	81.4	86.6
412	765 and 865	89.7	95.4	98.4	91.9	94.6	96.6
	1000 and 1240	61.6	79.0	91.3	91.9	94.3	96.2
	1240 and 1640	68.1	81.6	91.7	83.3	88.8	92.1
	1240 and 2130	44.0	66.1	84.2	73.9	80.6	85.8
	1640 and 2130	18.8	38.1	63.0	69.0	77.9	82.7
443	765 and 865	92.9	96.9	98.6	92.4	94.6	96.6
	1000 and 1240	63.0	79.9	91.5	91.3	93.8	95.9
	1240 and 1640	69.9	82.3	91.6	82.8	87.8	91.3
	1240 and 2130	45.1	67.3	84.2	74.7	80.6	85.2
	1640 and 2130	19.0	38.2	62.8	66.7	77.6	82.3
490	765 and 865	93.6	97.1	98.7	92.5	94.6	96.6
	1000 and 1240	69.2	83.0	92.8	90.9	93.3	95.4
	1240 and 1640	74.4	85.0	92.5	82.2	86.6	90.4
	1240 and 2130	50.2	71.1	86.0	75.1	80.1	84.6
	1640 and 2130	22.3	40.3	64.9	66.3	77.3	81.7
510	765 and 865	96.0	97.9	98.8	92.7	94.7	96.7
	1000 and 1240	69.9	83.8	93.2	90.8	93.2	95.4
	1240 and 1640	75.0	85.6	92.6	82.3	86.4	90.2
	1240 and 2130	51.7	71.9	86.2	75.4	80.2	84.5
	1640 and 2130	23.1	40.9	65.4	67.0	77.4	81.7
555	765 and 865	97.7	98.4	98.8	93.6	95.3	96.8
	1000 and 1240	76.3	87.7	95.0	90.4	93.1	95.2
	1240 and 1640	79.5	87.8	93.7	83.1	86.2	89.9
	1240 and 2130	59.9	76.3	88.4	76.8	81.1	84.8
	1640 and 2130	27.0	44.2	68.9	66.5	78.0	82.0

aerosol reflectance from the NIR (or SWIR) band, and (b) the aerosol reflectance dispersion provided between two NIR or SWIR bands. Obviously the aerosol reflectance can usually be more accurately extrapolated for the shorter wavelength distance than for the longer one. Thus the NIR method generally produces slightly better results than those from the SWIR methods. On the other hand, a larger dispersion of the aerosol reflectance between two NIR (or SWIR) bands with various aerosol models for atmospheric correction has a better sensitivity in deriving aerosol optical properties, leading to a better result in the derived water-leaving reflectances. For example, the SWIR method using bands 1240 and 2130 nm performed much better than that using bands 1640 and 2130 nm because the range of $\varepsilon(1240, 2130)$ for various aerosol models is significantly larger than that of $\varepsilon(1640, 2130)$, e.g., 0.98–4.76 versus 1.04–2.46 in Fig. 2.

In summary, except for the method using the SWIR bands of 1640 and 2130 nm, the atmospheric correction algorithm using the three SWIR band combinations (1000 and 1240 nm, 1240 and 1640 nm, and 1240 and 2130 nm) can produce results comparable with those from the NIR band method for cases of nonabsorbing and weakly absorbing aerosols.

C. Algorithm Evaluation for the Retrieved Aerosol Products

Aerosol optical property data over ocean can also be derived from the atmospheric correction procedure by converting the derived aerosol reflectance $\rho_A(\lambda)$ at the NIR or SWIR bands to the aerosol optical property products, e.g., aerosol optical thickness $\tau_a(865)$ and the Ångström exponent $\alpha(510, 865)$ from 510 and 865 nm.[1,40] SeaWiFS has been routinely producing the aerosol products $\tau_a(865)$ and $\alpha(510, 865)$ over the global ocean since its launch in September, 1997 and providing useful data products to study aerosol climatic forcing and radiative effects in the global and regional scales.[40,48,49]

The performances of the aerosol retrieval algorithm using various combinations of the SWIR bands are evaluated and compared with that using the NIR bands. Figure 7 shows the comparison results of the accuracy in the derived aerosol products with the aerosol retrieval algorithm using the NIR and various combinations of the SWIR bands. Figures 7(a) and 7(b) provide the results of the histogram as a function of the ratio value (derived over true value) in $\tau_a(865)$ for the aerosol model of the M80 and the T80,

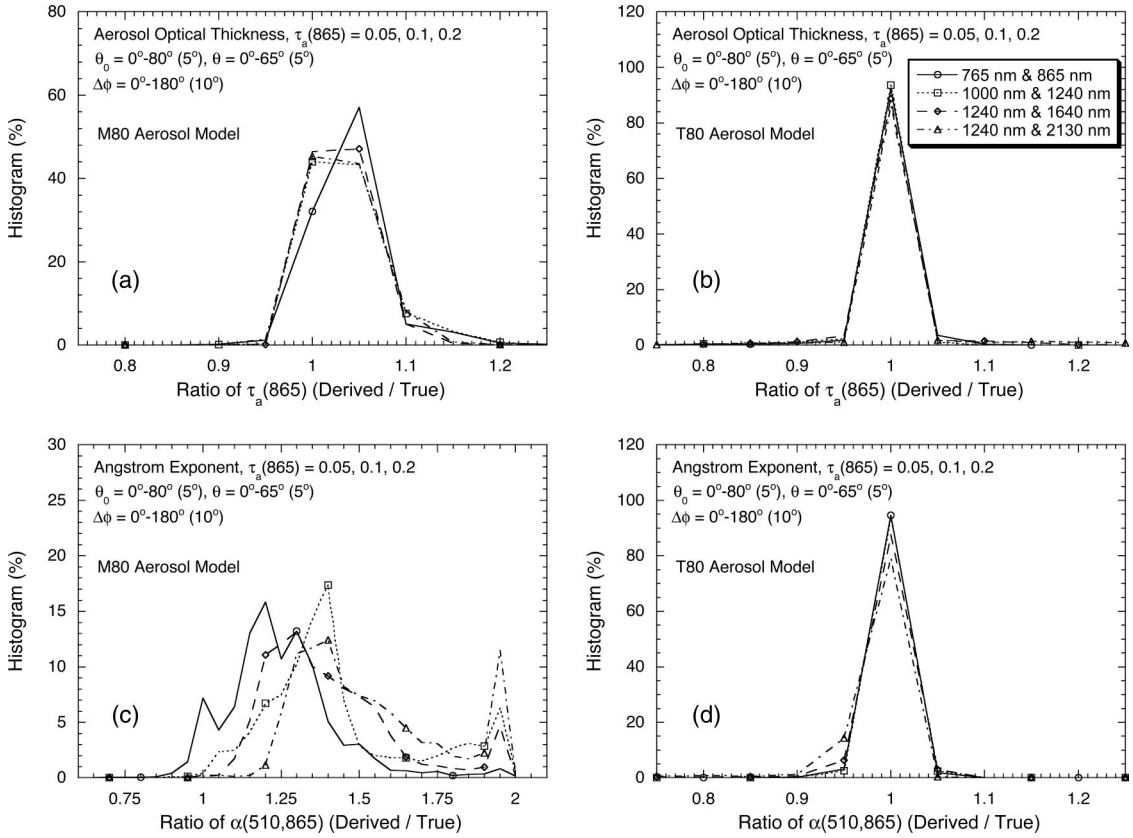

Fig. 7. Histogram as a function of the ratio value (derived over true value) in the aerosol parameter with the algorithm performed using the band combinations of 765 and 865 nm, 1000 and 1240 nm, 1240 and 1640 nm, and 1240 and 2130 nm for (a) and (b) ratio in the aerosol optical thickness $\tau_a(865)$ with the M80 and T80 model, respectively, and (c) and (d) ratio in the Ångström exponent $\alpha(510, 865)$ with the M80 and T80 models, respectively.

respectively, while Figs. 7(c) and 7(d) are the results of histogram as a function of the ratio value (derived over true) in Ångström exponent $\alpha(510, 865)$ for the M80 and the T80 model, respectively. In Fig. 7, the results in each plot include simulations that are carried out for the aerosol optical thicknesses $\tau_a(865)$ of 0.05, 0.1, and 0.2 (for the M80 or T80 model) and for the solar-zenith angles from 0° to 80° at steps of 5°, the sensor-zenith angles from 0° to 65° at steps of 5°, and the relative-azimuth angles from 0° to 180° at steps of 10°. Figure 7 compares the results that are derived from the aerosol retrieval algorithm using four options of the band combinations, i.e., 765 and 865 nm, 1000 and 1240 nm, 1240 and 1640 nm, and 1240 and 2130 nm. The results in Fig. 7 show that aerosol products can be derived as accurately from the three combinations of the SWIR bands as from the two NIR bands. The results from the NIR and the SWIR methods are comparable. For the T80 model, excellent retrievals are obtained for both $\tau_a(865)$ and $\alpha(510, 865)$ for all the methods. For the M80 aerosols, however, errors in $\tau_a(865)$ are usually within ~5%–10%, while errors in $\alpha(510, 865)$ are usually approximately 25%–40%. However, it is noted that $\alpha(510, 865)$ values for the M80 and the T80 models are 0.21 and 1.43 corresponding to large and small aerosol particles, respectively. Therefore, errors in $\alpha(510, 865)$ as in difference (not in relative) are similar for both the M80 and the T80 models. However, it is important to note that for the turbid waters in the coastal regions, the SWIR algorithm for aerosol retrievals should perform better than the NIR algorithm because of an invalid NIR black ocean assumption with the NIR algorithm.

4. Band Noise Effects

Because of the significantly low signal partition from ocean contribution in the sensor-measured TOA radiance, atmospheric correction for ocean color products is very sensitive to sensor spectral band errors from calibration,[50–53] as well as from sensor band noises, e.g., digitization noise[54] and sensor radiometric noise. The sensor spectral band radiometric performance can be characterized from a parameter such as the noise equivalent reflectance ($NE\Delta\rho$) or the more commonly used the SNR. Here we define SNR = $\rho_t(\lambda)/NE\Delta\rho(\lambda)$ for a given $\rho_t(\lambda)$ value. The value of the $NE\Delta\rho$ is more directly related to the sensor radiometric performance, whereas the SNR value depends not only on the sensor radiometric performance but also on the atmospheric and ocean optical and radiative properties, as well as the solar-sensor geometry.

To understand the band noise effects on the derived water-leaving reflectance spectra, simulations have

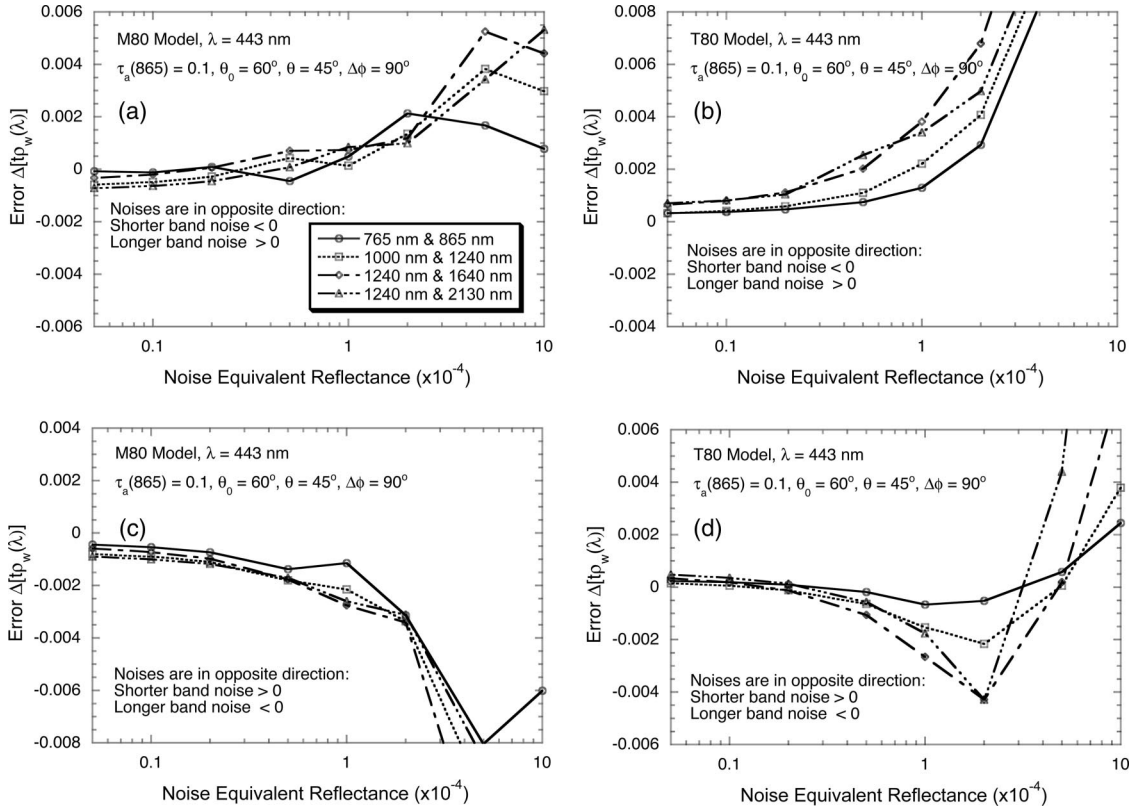

Fig. 8. Error in the derived water-leaving reflectance $[t\rho_w(\lambda)]$ at wavelength 443 nm as a function of NEΔρ for the algorithm performed using band combinations of 765 and 865 nm, 1000 and 1240 nm, 1240 and 1640 nm, and 1240 and 2130 nm and for cases of (a) and (b) that the shorter band NEΔρ < 0 and the longer band NEΔρ > 0 with the M80 and T80 models, respectively, and (c) and (d) that the shorter band NEΔρ > 0 and the longer band NEΔρ < 0 with the M80 and T80 models, respectively.

been carried out for the atmospheric correction using the NIR and various combinations of the SWIR bands with inclusion of the sensor noises. For the atmospheric correction using the NIR (or SWIR) bands, it has been demonstrated that the errors in the two NIR bands with opposite signs, e.g., the shorter band has calibration error biased low and the longer band has error biased high, lead to significantly larger uncertainties in the derived water-leaving reflectance spectra.[51,53] Thus simulations have been carried out only for cases with noises that are in the opposite signs to the two NIR and SWIR bands (the worst cases). Figure 8 provides an example of the noise effects at the NIR or SWIR bands for the atmospheric correction on the derived water-leaving reflectance. Figures 8(a) and 8(b) are errors in the derived water-leaving reflectance $\Delta[t\rho_w(\lambda)]$ at the wavelength 443 nm for the M80 and the T80 model, respectively, as a function of NEΔρ for which the shorter NIR (or SWIR) band has NEΔρ < 0, and the longer NIR (or SWIR) band has NEΔρ > 0. Figures 8(c) and 8(d) are the same as in Figs. 8(a) and 8(b) except that now the shorter NIR (or SWIR) band has NEΔρ > 0, and the longer NIR (or SWIR) band has NEΔρ < 0. This is for a specific case with aerosol optical thickness $\tau_a(865)$ of 0.1 and for the solar-zenith angle of 60°, the sensor-zenith angle of 45°, and the relative-azimuth angle of 90°. Each plot in Fig. 8 has four curves corresponding to the results of atmospheric correction that was performed using the band combinations of 765 and 865 nm, 1000 and 1240 nm, 1240 and 1640 nm, and 1240 and 2130 nm, respectively. In addition, the noise NEΔρ has been assumed to have the same magnitude (but the opposite sign) for the two NIR or SWIR bands used for the atmospheric correction.

Figure 8 shows that the error $\Delta[t\rho_w(\lambda)]$ converges as the NEΔρ value decreases. For the two NIR bands, the $\Delta[t\rho_w(\lambda)]$ value reaches the required accuracy for the NEΔρ of $\sim 10^{-4}$. For the combinations of the SWIR bands, the $\Delta[t\rho_w(\lambda)]$ value reaches the required accuracy for the M80 model at the NEΔρ of $\sim 8 \times 10^{-5}$ for all three SWIR band options, while for the T80 model the $\Delta[t\rho_w(\lambda)]$ results converge at the NEΔρ of $\sim 8 \times 10^{-5}$ for the 1000 and 1240 nm option and, they converge at the NEΔρ of $\sim 5 \times 10^{-5}$ for both the 1240 and 1640 nm and the 1240 and 2130 nm options. Table 2 provides the required NEΔρ (minimum requirements) and corresponding SNR values for the NIR and SWIR bands for the M80 aerosol model with various aerosol optical thicknesses for the case of the solar-zenith angle of 60°, the sensor-zenith angle of 45°, and the relative-azimuth angle of 90°. Obviously, the SNR values depend on the aerosol optical properties (model and aerosol optical thickness) as well as the solar-sensor geometry. Therefore, for the M80 model

Table 2. Required NEΔρ and Corresponding SNR Values for the NIR and SWIR Bands[a]

Cases		Required NEΔρ and Corresponding SNR at Given Band					
		765 nm	865 nm	1000 nm	1240 nm	1640 nm	2130 nm
NEΔρ		10^{-4}	10^{-4}	8×10^{-5}	8×10^{-5}	8×10^{-5}	8×10^{-5}
SNR for	0.05	229	157	133	85	58	38
M80 with	0.10	290	215	201	148	113	81
$\tau_a(865)$	0.20	426	345	356	290	238	183

[a]These values are for the M80 model with various aerosol optical thicknesses for the case of the solar-zenith angle of 60°, sensor-zenith angle of 45°, and relative-azimuth angle of 90°.

with $\tau_a(865)$ of 0.1, the required SNR values for 765, 865, 1000, 1240, 1640, and 2130 nm are approximately 290, 215, 201, 148, 113, and 81, respectively. For a reference in the comparisons, with the M80 model and the $\tau_a(865)$ of 0.1, the MODIS SNR values (based on MODIS specifications) for the two NIR ocean bands 748 and 869 nm are 341 and 272, respectively, while they are 12, 12, and 11 for the three SWIR bands at 1240, 1640, and 2130 nm, respectively. The MODIS SWIR bands are designed for atmospheric and land applications with normally significantly high TOA reflectances over the clouds and land at these wavelengths. The low SNR values in the MODIS SWIR bands, however, lead to significant noises in the retrieved NIR ocean water-leaving reflectances.[19]

5. Conclusions

Simulations have been carried out to evaluate and compare the performance of atmospheric correction using the NIR bands and the various combinations of the SWIR bands for retrieval of the water-leaving reflectance spectra from the UV (340 nm) to the visible wavelengths, as well as for deriving aerosol optical property products. The simulations show that atmospheric correction using the SWIR combinations of 1000 and 1240 nm, 1240 and 1640 nm, and 1240 and 2130 nm can generally produce results comparable with those using the NIR bands (765 and 865 nm). In particular, the water-leaving reflectance at the UV band (340 nm) can be derived accurately using the NIR bands as well as various combinations of the SWIR bands. Furthermore, it is also concluded from simulations that the performances of the aerosol retrieval algorithm using various combinations of the SWIR bands are comparable with that using the NIR bands. The aerosol optical thickness $\tau_a(865)$ can usually be retrieved within an accuracy of ~5%–10% [or ± 0.01 for small $\tau_a(865)$ values], while the error in the Ångström exponent $\tau(510, 865)$ is generally $\sim \pm 0.1$ in value. For the turbid waters in the coastal regions, however, the SWIR algorithm should produce better results than those from the NIR algorithm because the NIR algorithm has an incorrect assumption of the black ocean at the NIR bands and thus an overestimation of the aerosol contributions.

A sensitivity study has been conducted to evaluate the required sensor radiometric performance for the NIR and SWIR bands for the ocean color remote sensing. Results show that to accurately derive the water-leaving reflectance spectra, the required NEΔρ value at the solar-zenith angle of 60° for two NIR bands at 765 and 865 nm is $\sim 10^{-4}$, while the required NEΔρ values for 1000 and 1240 nm are $\sim 8 \times 10^{-5}$, and for 1640 and 2130 nm they are $\sim 5 \times 10^{-5}$. For the case of the M80 model with $\tau_a(865)$ of 0.1 and for the solar-zenith angle of 60°, the sensor-zenith angle of 45°, and the relative-azimuth angle of 90°, these NEΔρ values correspond to the SNR values of approximately 290, 215, 201, 148, 113, and 81 for bands of 765, 865, 1000, 1240, 1640, and 2130 nm, respectively.

The author thanks Chuck McClain for his encouragement at the beginning of this work in 2003 when the author was with University of Maryland, Baltimore County, and NASA Goddard Space Flight Center. This research was supported by NASA grants NNG05HL40I and NNG05HL35I and National Oceanic and Atmospheric Administration NPOESS Internal Government Studies (IGS) funding D2NF1NP. The views, opinions, and findings contained in this paper are those of the author and should not be construed as an official NOAA or U.S. Government position, policy, or decision.

References

1. H. R. Gordon and M. Wang, "Retrieval of water-leaving radiance and aerosol optical thickness over the oceans with SeaWiFS: A preliminary algorithm," Appl. Opt. **33,** 443–452 (1994).
2. H. R. Gordon, "Atmospheric correction of ocean color imagery in the Earth Observing System era," J. Geophys. Res. **102,** 17081–17106 (1997).
3. H. R. Gordon, J. W. Brown, and R. H. Evans, "Exact Rayleigh scattering calculations for use with the Nimbus-7 Coastal Zone Color Scanner," Appl. Opt. **27,** 862–871 (1988).
4. H. R. Gordon and M. Wang, "Surface roughness considerations for atmospheric correction of ocean color sensors. 1: The Rayleigh scattering component," Appl. Opt. **31,** 4247–4260 (1992).
5. M. Wang, "The Rayleigh lookup tables for the SeaWiFS data processing: accounting for the effects of ocean surface roughness," Int. J. Remote Sens. **23,** 2693–2702 (2002).
6. M. Wang, "A refinement for the Rayleigh radiance computation with variation of the atmospheric pressure," Int. J. Remote Sens. **26,** 5651–5663 (2005).
7. P. Y. Deschamps, M. Herman, and D. Tanre, "Modeling of the atmospheric effects and its application to the remote sensing of ocean color," Appl. Opt. **22,** 3751–3758 (1983).
8. H. Yang and H. R. Gordon, "Remote sensing of ocean color: assessment of water-leaving radiance bidirectional effects on

atmospheric diffuse transmittance," Appl. Opt. **36,** 7887–7897 (1997).
9. R. S. Fraser, S. Mattoo, E. N. Yeh, and C. R. McClain, "Algorithm for atmospheric and glint corrections of satellite measurements of ocean pigment," J. of Geophys. Res. **102,** 17107–17118 (1997).
10. M. Wang and S. Bailey, "Correction of the sun glint contamination on the SeaWiFS ocean and atmosphere products," Appl. Opt. **40,** 4790–4798 (2001).
11. R. Frouin, M. Schwindling, and P. Y. Deschamps, "Spectral reflectance of sea foam in the visible and near-infrared: *in situ* measurements and remote sensing implications," J. Geophys. Res. **101,** 14361–14371 (1996).
12. H. R. Gordon and M. Wang, "Influence of oceanic whitecaps on atmospheric correction of ocean-color sensor," Appl. Opt. **33,** 7754–7763 (1994).
13. K. D. Moore, K. J. Voss, and H. R. Gordon, "Spectral reflectance of whitecaps: their contribution to water-leaving radiance," J. Geophys. Res. **105,** 6493–6499 (2000).
14. C. R. McClain, G. C. Feldman, and S. B. Hooker, "An overview of the SeaWiFS project and strategies for producing a climate research quality global ocean bio-optical time series," Deep-Sea Res., Part II **51,** 5–42 (2004).
15. V. V. Salomonson, W. L. Barnes, P. W. Maymon, H. E. Montgomery, and H. Ostrow, "MODIS: advanced facility instrument for studies of the Earth as a system," IEEE Trans. Geosci. Remote Sens. **27,** 145–152 (1989).
16. D. A. Siegel, M. Wang, S. Maritorena, and W. Robinson, "Atmospheric correction of satellite ocean color imagery: the black pixel assumption," Appl. Opt. **39,** 3582–3591 (2000).
17. R. P. Stumpf, R. A. Arnone, R. W. Gould, P. M. Martinolich, and V. Ransibrahmanakul, *A Partially Coupled Ocean-Atmosphere Model for Retrieval of Water-Leaving Radiance from SeaWiFS in Coastal Waters,* NASA Tech. Memo. 2003–206892, S. B. Hooker and E. R. Firestone, eds. (NASA Goddard Space Flight Center, 2003), Vol. 22.
18. K. G. Ruddick, F. Ovidio, and M. Rijkeboer, "Atmospheric correction of SeaWiFS imagery for turbid coastal and inland waters," Appl. Opt. **39,** 897–912 (2000).
19. M. Wang and W. Shi, "Estimation of ocean contribution at the MODIS near-infrared wavelengths along the east coast of the U.S.: two case studies," Geophys. Res. Lett. **32,** L13606, doi: 13610.11029/12005GL022917 (2005).
20. R. A. Arnone, P. Martinolich, R. W. Gould, M. Sydor, and R. P. Stumpf, "Coastal optical properties using SeaWiFS," in *Ocean Optics XIV* (Office of Naval Research, 1998).
21. R. W. Gould, R. A. Arnone, and P. M. Martinolich, "Spectral dependence of the scattering coefficient in Case-1 and Case-2 waters," Appl. Opt. **38,** 2377–2383 (1999).
22. S. J. Lavender, M. H. Pinkerton, G. F. Moore, J. Aiken, and D. Blondeau-Patissier, "Modification to the atmospheric correction of SeaWiFS ocean color images over turbid waters," Cont. Shelf Res. **25,** 539–555 (2005).
23. G. M. Hale and M. R. Querry, "Optical constants of water in the 200 nm to 200 μm wavelength region," Appl. Opt. **12,** 555–563 (1973).
24. L. Kou, D. Labrie, and P. Chylek, "Refractive indices of water and ice in the 0.65–2.5 μm spectral range," Appl. Opt. **32,** 3531–3540 (1993).
25. R. R. Li, Y. J. Kaufman, B. C. Gao, and C. O. Davis, "Remote sensing of suspended sediments and shallow coastal waters," IEEE Trans. Geosci. Remote Sens. **41,** 559–566 (2003).
26. M. Wang and W. Shi, "Cloud masking for ocean color data processing in the coastal regions," IEEE Trans. Geosci. Remote Sens. **44,** 3196–3205 (2006).
27. B. C. Gao, M. J. Montes, Z. Ahmad, and C. O. Davis, "Atmospheric correction algorithm for hyperspectral remote sensing of ocean color from space," Appl. Opt. **39,** 887–896 (2000).
28. Z. P. Lee, K. L. Carder, and R. A. Arnone, "Deriving inherent optical properties from water color: a multiple quasi-analytical algorithm for optically deep waters," Appl. Opt. **41,** 5755–5772 (2002).
29. S. Maritorena, D. A. Siegel, and A. Peterson, "Optimization of a semi-analytical ocean color model for global scale applications," Appl. Opt. **41,** 2705–2714 (2002).
30. J. E. O'Reilly, S. Maritorena, B. G. Mitchell, D. A. Siegel, K. L. Carder, S. A. Garver, M. Kahru, and C. R. McClain, "Ocean color chlorophyll algorithms for SeaWiFS," J. Geophys. Res. **103,** 24937–24953 (1998).
31. W. E. Esaias, M. R. Abbott, I. Barton, O. B. Brown, J. W. Campbell, K. L. Carder, D. K. Clark, R. L. Evans, F. E. Hodge, H. R. Gordon, W. P. Balch, R. Letelier, and P. J. Minnet, "An overview of MODIS capabilities for ocean science observations," IEEE Trans. Geosci. Remote Sens. **36,** 1250–1265 (1998).
32. C. S. Roesler, M. J. Perry, and K. L. Carder, "Modeling *in situ* phytoplankton absorption from total absorption spectra in productive inland marine waters," Limnol. Oceanogr. **34,** 1510–1523 (1989).
33. A. Bricaud, A. Morel, and L. Prieur, "Absorption by dissolved organic matter in the sea (yellow substance) in the UV and visible domains," Limnol. Oceanogr. **28,** 43–53 (1981).
34. M. S. Twardowski, E. Boss, J. M. Sullivan, and P. L. Donaghay, "Modeling the spectral shape of absorption by chromophoric dissolved organic matter," Mar. Chem. **89,** 69–88 (2004).
35. O. Torres, J. R. Herman, Z. Ahmad, and J. Gleason, "Derivation of aerosol properties from satellite measurements of backscattered ultraviolet radiation: theoretical basis," J. Geophys. Res. **103,** 17099–17110 (1998).
36. F. X. Kneizys, E. P. Shettle, L. W. Abreu, J. H. Chetwynd, G. P. Anderson, W. O. Gallery, J. E. A. Selby, and S. A. Clough, *Users Guide to LOWTRAN-7* (Air Force Geophysics Laboratory, AFGL-TR-88-0177, 1988).
37. NOAA, NASA, and USAF, *U.S. Standard Atmosphere, 1976* (U.S. Government Printing Office, 1976), p. 227.
38. S. W. Bailey and P. J. Werdell, "A multisensor approach for the on-orbit validation of ocean color satellite data products," Remote Sens. Environ. **102,** 12–23 (2006).
39. G. Zibordi, F. Melin, and J.-F. Berthon, "Comparison of SeaWiFS, MODIS, and MERIS radiometric products at a coastal site," Geophys. Res. Lett. **33,** L06617, doi:06610.01029/02006GL025778 (2006).
40. M. Wang, K. D. Knobelspiesse, and C. R. McClain, "Study of the Sea-Viewing Wide Field-of-View Sensor (SeaWiFS) aerosol optical property data over ocean in combination with the ocean color products," J. Geophys. Res. **110,** D10S06, doi:10.1029/2004JD004950 (2005).
41. M. Wang, "Aerosol polarization effects on atmospheric correction and aerosol retrievals in ocean color remote sensing," Appl. Opt. (to be published).
42. E. P. Shettle and R. W. Fenn, *Models for the Aerosols of the Lower Atmosphere and the Effects of Humidity Variations on Their Optical Properties* U.S. Air Force Geophysics Laboratory (AFGL-TR-79-0214, 1979).
43. K. D. Knobelspiesse, C. Pietras, G. S. Fargion, M. Wang, R. Frouin, M. A. Miller, A. Subramaniam, and W. M. Balch, "Maritime aerosol optical properties measured by handheld sun photometers," Remote Sens. Environ. **93,** 87–106 (2004).
44. M. Schwindling, P. Y. Deschamps, and R. Frouin, "Verification of aerosol models for satellite ocean color remote sensing," J. Geophys. Res. **103,** 24919–24935 (1998).
45. A. Smirnov, B. N. Holben, Y. J. Kaufman, O. Dubovik, T. F. Eck, I. Slutsker, C. Pietras, and R. N. Halthore, "Optical properties of atmospheric aerosol in maritime environments," J. Atmos. Sci. **59,** 501–523 (2002).

46. M. Wang, "Extrapolation of the aerosol reflectance from the near-infrared to the visible: the single-scattering epsilon vs multiple-scattering epsilon method," Int. J. Remote Sens. **25,** 3637–3650 (2004).
47. M. Wang and H. R. Gordon, "A simple, moderately accurate, atmospheric correction algorithm for SeaWiFS," Remote Sens. Environ. **50,** 231–239 (1994).
48. M. D. Chou, P. K. Chan, and M. Wang, "Aerosol radiative forcing derived from SeaWiFS-retrieved aerosol optical properties," J. Atmos. Sci. **59,** 748–757 (2002).
49. M. Wang, S. Bailey, and C. R. McClain, "SeaWiFS provides unique global aerosol optical property data," Eos Trans. Am. Geophys. Union **81,** 197 and 202 (2000).
50. R. H. Evans and H. R. Gordon, "CZCS system calibration: A retrospective examination," J. Geophys. Res. **99,** 7293–7307 (1994).
51. H. R. Gordon, "In-orbit calibration strategy for ocean color sensors," Remote Sens. Environ. **63,** 265–278 (1998).
52. J. R. E. Eplee, W. D. Robinson, S. W. Bailey, D. K. Clark, P. J. Werdell, M. Wang, R. A. Barnes, and C. R. McClain, "Calibration of SeaWiFS. II: Vicarious techniques," Appl. Opt. **40,** 6701–6718 (2001).
53. M. Wang and H. R. Gordon, "Calibration of ocean color scanners: how much error is acceptable in the near-infrared?" Remote Sens. Environ. **82,** 497–504 (2002).
54. C. Hu, K. L. Carder, and F. E. Muller-Karger, "How precise are SeaWiFS ocean color estimates? Implications of digitization-noise errors," Remote Sens. Environ. **76,** 239–249 (2001).